

## Iron oxides as a cause of GPR reflections

Remke L. Van Dam\*, Wolfgang Schlager<sup>†</sup>, Mark J. Dekkers\*\*,  
and Johan A. Huisman<sup>§</sup>

### ABSTRACT

Iron oxides frequently occur as secondary precipitates in both modern and ancient sediments and may form bands or irregular patterns. We show from time-domain reflectometry (TDR) field studies that goethite iron-oxide precipitates significantly lower the electromagnetic wave velocity of sediments. Measured variations in magnetic permeability do not explain this decrease. The TDR measurements and a dielectric mixing model also show that neither electrical conductivity nor relative permittivity of the solid material are altered significantly by the iron-oxide material. From drying during all of the measurements, the amount of iron oxides appears to correlate with the volumetric water content, which is the result of differences in water retention capacity between goethite and quartz. These variations in water content control relative permittivity and explain the observed variation in electromagnetic wave velocity. Using 2-D synthetic radar sections, we show that the pattern of iron-oxide precipitation may have a profound influence on the GPR reflection configuration and can cause major difficulties in interpretation.

### INTRODUCTION

Over the last decade, the interest in ground-penetrating radar (GPR) as a tool to investigate the shallow subsurface has widened. During this period, theoretical research mainly focussed on synthetic modeling of wave propagation (e.g., Carcione, 1998). Studies combining wave theory and geological or petrophysical data have been sparse, and there is a lack of understanding of several features in field data, such as the impact of iron oxides on GPR waves. Recently, layers rich in iron oxides were identified as possible GPR reflectors by Van

Dam and Schlager (2000). They used time-domain reflectometry (TDR) and sedimentological analyses to show in a qualitative way that iron oxides significantly lower the electromagnetic wave velocity of sediments. The purpose of this paper is to quantify this relationship in order to understand why and how iron-oxide precipitates influence the electromagnetic field, and to establish the possible implications for GPR records.

Several field and laboratory studies show that iron oxides can have a profound influence on electromagnetic wavefields in general (Robinson et al., 1994; Klein and Santamarina, 2000), magnetic susceptibility (e.g., Mullins, 1977), or attenuation (Mätzler, 1998). Iron-oxide precipitates are found in various chemical forms in a wide range of depositional and climatic environments (Driessen and Dudal, 1991). Iron is easily soluble under reducing conditions, and easily transported after reduction to  $\text{Fe}^{2+}$ . Oxidation towards  $\text{Fe}^{3+}$  and subsequent precipitation of ferrous compounds occurs once oxygen levels are sufficiently high. The pattern of precipitation often reflects the hydraulic properties of the sediment, such that a fluctuating groundwater level can lead to “ferricrete” horizons cemented by iron oxide (Cornell and Schwertmann, 1996), whereas roots may cause irregular patterns of iron-oxide precipitation.

In this paper, we try to understand why iron-oxide precipitates lower the electromagnetic wave velocity of sediments. We sampled sediment with varying degrees of iron-oxide content in a quarry in The Netherlands, and analyzed the characteristics of the sediment using grain size analysis, scanning electron microscopy (SEM), chemical analyses by inductively coupled plasma atomic-emission spectrometry (ICP-AES), and thermogravimetric techniques (TGA). We studied the effect of the iron oxides on all components of the electromagnetic field using magnetic measurements, TDR measurements, and dielectric mixing models. Finally, we used the information from these analyses to construct 2-D synthetic radar sections that illustrate the possible impact of iron-oxide precipitates on GPR reflections.

Manuscript received by the Editor April 5, 2000; revised manuscript received June 8, 2001.

\*Formerly Vrije Universiteit Amsterdam, Faculty of Earth Sciences, 1081 HV Amsterdam, The Netherlands; presently Bemuurde Weerd o.z. 7, 3514 AN Utrecht, The Netherlands. E-mail: remke@geopuls.nl.

<sup>†</sup>Vrije Universiteit Amsterdam, Faculty of Earth Sciences, De Boelelaan 1085, 1081 HV Amsterdam, The Netherlands. E-mail: schw@geo.vu.nl.

\*\*Utrecht University, Paleomagnetic Laboratory Fort Hoofddijk, Budapestlaan 17, 3584 CD Utrecht, The Netherlands. E-mail: dekkers@geo.uu.nl.

<sup>§</sup>University of Amsterdam, Institute for Biodiversity and Ecosystem Dynamics (IBED), Physical Geography, Nieuwe Achtergracht 166, 1018 WV Amsterdam, The Netherlands. E-mail: s.huisman@science.uva.nl.

© 2002 Society of Exploration Geophysicists. All rights reserved.

### THEORY

The GPR technique is based on the propagation and reflection of electromagnetic energy in the subsurface. The (frequency dependent) properties that play a role in the behavior of the electromagnetic energy in a medium are the dielectric permittivity ( $\epsilon$ ), where  $\epsilon = \epsilon_0 \epsilon_r$ ; the electrical conductivity ( $\sigma$ ); and the magnetic permeability ( $\mu$ ), where  $\mu = \mu_0 \mu_r$  (Von Hippel, 1954). Here,  $\epsilon_0$  is the permittivity of vacuum ( $8.85419 \times 10^{-12}$  F/m),  $\epsilon_r$  is the relative permittivity,  $\mu_0$  is the magnetic permeability of vacuum ( $4\pi \times 10^{-7}$  H/m), and  $\mu_r$  is the relative magnetic permeability. Together, these properties define the impedance ( $Z$ ) of the medium (Brewster and Annan, 1994):

$$Z = \left( \frac{j\omega\mu}{\sigma + j\omega\epsilon} \right)^{1/2}, \quad (1)$$

where  $j = \sqrt{-1}$  and  $\omega = 2\pi f$  is angular frequency (radians/second). We do not consider complex permittivity caused by water dipole relaxation because its frequency is above our bandwidth.

The propagation velocity ( $v$ ) of electromagnetic waves in a medium is found by

$$v = \frac{c_0}{\left[ \epsilon_r \mu_r \left( \frac{1 + \sqrt{1 + \tan^2 \delta}}{2} \right) \right]^{1/2}}, \quad (2)$$

where  $c_0$  is the electromagnetic wave velocity in vacuum ( $3 \times 10^8$  m/s) and  $\tan \delta$  is the loss tangent. The loss tangent, which is controlled by the conductivity ( $\sigma$ ) (Von Hippel, 1954), approaches zero for low-loss material, such as sand. Consequently, the velocity is mainly controlled by  $\epsilon_r$  and  $\mu_r$ .

When a propagating electromagnetic wave encounters a discontinuity in electric, magnetic or conductive properties, part of the electromagnetic energy is reflected. The reflection strength is proportional to the magnitude of change in dielectric properties. For a perpendicular incident wave the reflection coefficient ( $R$ ) is expressed as

$$R = \frac{Z_2 - Z_1}{Z_2 + Z_1}, \quad (3)$$

where  $Z_1$  and  $Z_2$  are the impedances of the layers above and below the discontinuity, respectively (Brewster and Annan, 1994). The dielectric permittivity, which is generally controlled by volumetric water content ( $\theta$ ), is assumed to play a dominant role in the reflection process and propagation of electromagnetic waves (Sutinen, 1992; Huggenberger, 1993). The electrical conductivity ( $\sigma$ ) of a material depends on the amount of kinetic energy that is irreversibly converted into heat (Van Der Kruk et al., 1999) and controls, together with  $\epsilon_r$ , the attenuation of an electromagnetic wave (e.g., Daniels et al., 1988). Magnetic permeability, which is the third factor influencing the impedance [equation (1)], is generally assumed to be near unity (e.g., Brewster and Annan, 1994; Carcione, 1998; Daniels et al., 1988). A range of typical electromagnetic properties for common geologic materials was given by Davis and Annan (1989).

### METHODS

#### Time-domain reflectometry

TDR is widely used to measure the water content of soils. The TDR method uses empirical relationships between the relative

permittivity ( $\epsilon_r$ ) and volumetric water content ( $\theta$ ) (e.g., Topp et al., 1980), under the assumption that  $\mu_r$  is equal to 1. The method is based on the propagation velocity of a guided electromagnetic signal in sediment (e.g., Brisco et al., 1992). For the measurements, we used a three-rod probe with a length of 5 cm that was inserted into the sediment. The probe is connected to a Tektronix cable tester that transmits a fast-rise voltage pulse (bandwidth about 300 kHz–3 GHz) through the transmission line and probe. The waveform resulting from the reflection at the end of the probe is analyzed to obtain the traveltime ( $\Delta t_s$ ) of the pulse along the rods. This traveltime is used to calculate the velocity of the electromagnetic wave or can be used to obtain  $\epsilon_r \mu_r$  from the formula (Roth et al., 1990)

$$\epsilon_r \mu_r = \left( \frac{c_0 \Delta t_s}{2L_p} \right)^2, \quad (4)$$

where  $L_p$  is the length of the probe (m). Later, we use the quantity  $\epsilon_r \mu_r$  instead of velocity to present and discuss the TDR results. This facilitates comparison with  $\epsilon_r$  values that are commonly used in TDR and GPR literature.

Dielectric mixing models are frequently used to analyze the contribution of the different sediment constituents (solid, liquid, and gas phase) to  $\epsilon_r$  (e.g., Tinga et al., 1973). Under the assumption that  $\mu_r$  is equal to 1, a simple three-phase model can be used for humid samples (Bohl and Roth, 1994):

$$\epsilon_r = (\theta \cdot \epsilon_w^\alpha + (1 - \eta) \epsilon_s^\alpha + (\eta - \theta) \epsilon_a^\alpha)^{1/\alpha}, \quad (5)$$

which reduces to a two-phase model for dry samples:

$$\epsilon_r = ((1 - \eta) \epsilon_s^\alpha + \eta \cdot \epsilon_a^\alpha)^{1/\alpha}, \quad (6)$$

where  $\eta$  is porosity,  $\epsilon_w$  is the relative permittivity of water (80),  $\epsilon_s$  is the relative permittivity of solid material,  $\epsilon_a$  is the relative permittivity of air (1), and  $\alpha$  is a constant [0.5 for isotropic and homogeneous material (Roth et al., 1990)].

TDR is also used to calculate the bulk electrical conductivity ( $\sigma_{DC}$ ) of sediment (Giese and Tieman, 1975). For this, the attenuation of the voltage pulse is estimated from the reflection coefficient at long times ( $\rho_\infty$ ) using  $R_{tot} = Z_c(1 + \rho_\infty/(1 - \rho_\infty))$ , where  $R_{tot}$  is the total resistance of sediment and equipment (ohms) and  $Z_c$  is the cable impedance (50 ohms). The bulk electrical conductivity can be calculated according to Huisman and Bouten (2000):

$$\sigma_{DC} = \frac{K_p}{R_{tot} - (L_c \cdot R_c + R_0)}, \quad (7)$$

where  $K_p$  is a probe constant,  $R_c$  is the resistance of the coaxial cable (ohms/meter),  $R_0$  is the resistance of the cable tester and connectors (ohms), and  $L_c$  is the cable length (meters). The calculated dc electrical conductivity is frequency independent but can be recalculated into a real conductivity (Ulriksen, 1982) using

$$\sigma = \sigma_{DC} + \omega \cdot \epsilon'', \quad (8)$$

where  $\epsilon''$  is the imaginary part of the permittivity.

#### Thermogravimetric analysis

Thermal analysis refers to the study of the behavior of materials as a function of temperature change. Thermogravimetric

(TG) analysis is a technique that measures the change in weight of a sample as a function of temperature. The shape of the TG curve gives information on sample composition, thermal characteristics of the sample, and on the products formed during heating (Blazek, 1973). Parts of the curve with zero slope indicate where the sample is stable for a certain temperature range. Nonzero slopes give the rate and direction of the weight change. The derivative (DTG) of the thermogravimetric curve shows the change in weight with time as a function of temperature or time.

### Magnetic measurements

In the low-intensity field region, the magnetization  $M$  is linear with the intensity of the applied field  $H$  (or  $B$ ) for all substances. Therefore, the initial or low-field magnetic susceptibility, defined as  $\chi = M/H$  or  $\chi = M \cdot \mu_0/B$ , is a material-specific property. The magnetic susceptibility is usually expressed per unit volume ( $\kappa$ ) and referred to as mass-specific susceptibility ( $\chi$ ) when expressed per unit mass. The applied field, initial susceptibility, and magnetic permeability are related as follows:

$$\mu = \frac{B}{H} = \mu_0(1 + \kappa), \quad (9)$$

and

$$\mu_r = \frac{\mu}{\mu_0} = 1 + \kappa. \quad (10)$$

For the mixed sediments we consider, magnetic interaction is not important, and the magnetic anisotropy (directional dependence of the initial susceptibility) is estimated to be <1%, so the measured  $\chi$  can be seen as the sum of the  $\chi$  s of individual minerals.

We used a bridge-type susceptometer (Jelinek, V., 1980, Agico Manual, Czech Republic), where the susceptibility of a sample is related to the imbalance between two coils, in one of which the sample is inserted. The field strength,  $H$ , applied by the instrument is 300 A/m at an operating frequency of 920 Hz. Our samples contain only iron oxides in small amounts, and we neglect any possible frequency dependence (Worm et al., 1993). From the instrument magnetic-susceptibility reading ( $R_\kappa$ ), the mass-specific susceptibility  $\chi$  can be calculated according to:

$$\chi = \frac{k \cdot V \cdot R_\kappa \times 10^{-6}}{m}, \quad (11)$$

where  $k$  is a range factor (0.05 for the present samples),  $V$  is the standard sample volume ( $10^{-5} \text{ m}^3$ ), and  $m$  is mass (kilograms). To convert mass specific to volume-specific susceptibility values, we used a specific density ( $\rho$ ) of  $2500 \text{ kg/m}^3$  in the formula  $\kappa = \chi \cdot \rho$ . According to equation (10),  $\kappa$  can now be used to calculate  $\mu_r$ , that is the input for the calculation of the impedance  $Z$  [equation (1)] and electromagnetic wave velocity [equation (2)].

### GPR modeling

Using TDR data, models of electromagnetic wave velocity in the subsurface can be constructed. These 2-D layer models form the input for pulseEKKO ray-trace modeling software (pulse EKKO synthetic radargram user's guide; Sensors & Software, 1996) that constructs synthetic GPR sections. The

program calculates spatially correct sections but does not include multiples and diffractions to the modeling. Each layer in the model is assigned a constant velocity and attenuation. We convolved a Ricker wavelet with the layer section impulse response function to form the synthetic traces.

## SAMPLING AND SEDIMENT DESCRIPTION

### Sampling and TDR tests

We obtained our data from moist eolian quartz sand of the Twente Formation in the Boudewijn quarry, Ossendrecht, The Netherlands (Figure 1a). We conducted TDR measurements for three profiles (Figure 1). Site 5a is made up of an orange zone for the upper 0.28 m, a red band, rich in iron oxides, for the next 0.08 m, and a white zone at the bottom. The TDR profile shows a baseline value for  $\epsilon_r \mu_r$  of around 6 in the orange and white sediment. At the position of the band rich in iron oxides, the  $\epsilon_r \mu_r$  values increase to around 9, thus causing a drop in electromagnetic wave velocity [equation (2)]. Site 8 is less pronounced in color differences, but has a reddish zone (0.35–0.55 m) between orange material. The TDR profile does not reveal an obvious trend related to the color changes. Site 11 consists of two orange zones (0–0.5 m and 1.5–2 m), a red zone (0.5–1.5 m), and a white zone for the lower 0.5 m. The TDR profile for this site shows a clear step in the  $\epsilon_r \mu_r$  value from around 5 to 6 at the change from orange to red sediment at 0.5 m. At a depth of 2.0 m, a sharp peak, related to a finer grained layer, is present. Due to the close water table, the  $\epsilon_r \mu_r$  curve does not return to lower values in the white material.

Using the red staining of the sediment, we identified three units: white, orange, and red. At an even distribution over the units, we took sample material at 14 specific locations and added 6 samples from bulk material (Figure 1). The samples have an average grain size of  $281 \mu\text{m}$ , with about 1.5% in the silt fraction (Table 1). The material is essentially clay free and contains no organic matter. SEM and energy dispersive X-ray spectra (EDX) show that the iron oxide is present as a thin coating around the grains. Using ICP-AES, we found the amount of iron in the sediments to range in abundance between 980.2 and 7050.1 ppm (Table 1). These values are for iron only since (iron) oxides cannot be defined from chemical methods such as ICP-AES. Nevertheless, these values represent relative proportions of the iron oxides in the different samples. The red samples form a distinct group with high iron contents, whereas the orange and white units with lower iron contents show some overlap.

### Thermogravimetric analysis

We conducted thermogravimetric analysis for 20 samples, with typical weights of 55 to 90 mg (Table 1), selected from the three units discussed before. The samples were heated from about 22 to  $943^\circ\text{C}$  at an average rate of  $10.2^\circ\text{C}/\text{min}$ . Figure 2 shows the results per unit as both TG curves and their derivatives (DTG). The TG curves show a strong weight loss between the start of the measurements and  $100^\circ\text{C}$ . This is caused by the evaporation of free water from the pores (Blazek, 1973; Földvari, 1991). The white and the red samples have an average weight loss of about 4 and 7%, respectively, whereas the orange samples occupy an intermediate position close to the white samples. The sharp peaks in the DTG curves at  $100^\circ\text{C}$  are

the result of some temperature fluctuation. An endothermic reaction due to the boiling of water, leading to an instantaneous heat release, causes this fluctuation.

In order to analyze and to be able to compare the thermal behavior of the samples for the temperature range above 100°C, we have corrected for the weight losses due to water evaporation. The results for these calculations show three weight-loss events (Figure 3), which have their maxima at about 280, 490, and 570°C, respectively. We calculated the losses in terms of percentage for the range 200–300°C for the first event and over the range 400–600°C for the second and third events (Table 1). The derivative curves never reach zero until about 750°C. This shows there is a small but continuous background weight loss on which the major events are superimposed. We attribute this weight loss to the gradual evaporation of adhesive water from the grain surface (De Marsily, 1986). The first weight-loss event causes a clear difference in curve shape between the white and the red samples, whereas the orange samples occupy an intermediate position. The white samples lack the presence of this event, whereas the red samples show a clear weight loss (Figure 3). The weight loss in the first event thus seems

to depend on the presence of iron oxides in the material. This event shows a very high correlation ( $R^2 = 0.97$ ) with the iron contents from the ICP-AES measurements (Table 1). The second weight-loss event has the same appearance in all three units, and its width and height in the DTG curves are comparable (Table 1). Possibly, this event is related to small amounts of clayey particles present in the sediment. The third weight-loss event at 570°C is small but present in all samples. This event is most likely caused by an endothermic reaction, related to the  $\alpha$ - $\beta$  transformation of quartz ( $\text{SiO}_2$ ), which is the main constituent of the sediment (Blazek, 1973).

**RESULTS—ELECTROMAGNETIC PROPERTIES**

**Magnetic measurements**

We measured mass-specific susceptibility ( $\chi$ ) for the 20 samples, both under field conditions (i.e., humid) and after drying at 45°C for 16 hours. The values ranged between  $-0.046 \times 10^{-8}$  and  $0.576 \times 10^{-8} \text{ m}^3/\text{kg}$  for the humid samples, and between  $0.001 \times 10^{-8}$  and  $0.767 \times 10^{-8} \text{ m}^3/\text{kg}$  for the dry samples (Table 2). The lower average susceptibility of the humid

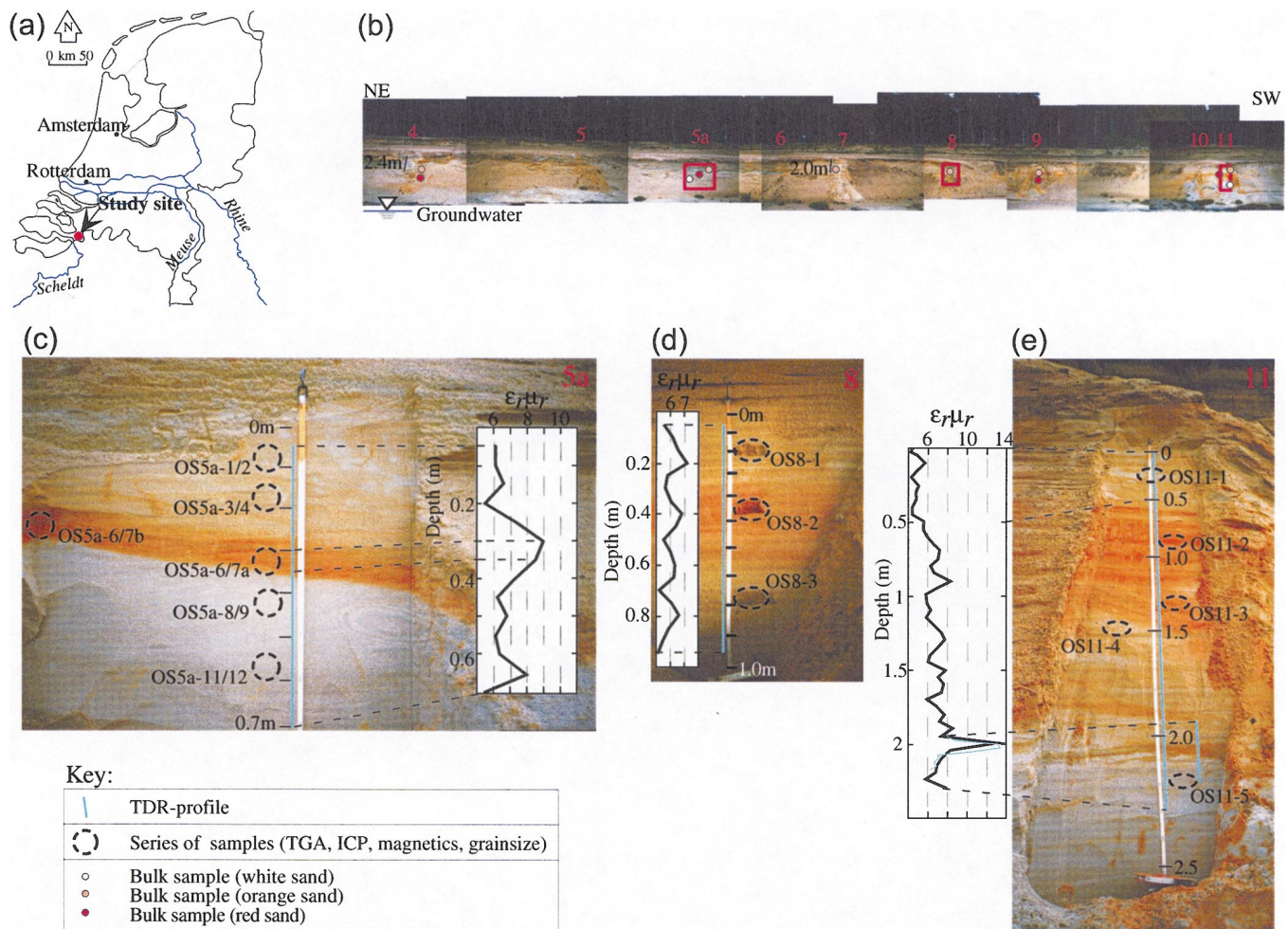


FIG. 1. Diagram showing locations of the study area and sampling points and the results of the TDR measurements: (a) The location of the study area in The Netherlands; (b) photomosaic of quarry face, showing the position of local groundwater level, bulk-sample locations, and rectangles referring to detailed sampling and TDR-measurement sites; (c) site 5a; (d) site 8; and (e) site 11. The TDR diagrams in (c), (d), and (e) plot  $\epsilon_r \mu_r$  against depth.

samples is caused by the diamagnetic water, having a negative  $\chi$ . Figure 4 summarizes the results for the three units in a plot of  $\mu_r$  against sample weight. The iron-oxide concentration appears to have a larger influence on  $\mu_r$  than does water. The offset on the vertical ( $\mu_r$ ) axis between a white (iron-oxide free) sample and a red sample (iron-oxide rich) is about three times the offset between a humid and a dry sample of the same unit. The calculated  $\mu_r$  values allow a clear distinction between the units, but the differences in  $\mu_r$  are too small to cause a significant contrast in  $Z$  [equation (3)].

### TDR measurements

In the laboratory, we used 200-cm<sup>3</sup> cylinders and 10-cm TDR probes to measure  $\varepsilon_r$  and  $\sigma_{DC}$  of the bulk sediment from the three different units (Figure 1). We filled three cylinders with humid sediment (A samples), and three other cylinders with dry sediment (B samples). We measured the A samples both under field conditions and after drying at 70°C for 14 hours. The volumetric water content ( $\theta$ ) for the A samples followed from the weight loss during drying ( $\Delta_w$ ) and the volume ( $V$ ) of the cylinder ( $\theta = \Delta_w/V$ ). We calculated the porosity from  $\eta = 1 - W_{dry}/\rho \cdot V$ , where  $W_{dry}$  is the dry weight and  $\rho$  is the density of quartz (2500 kg/m<sup>3</sup>). The difference in porosity between the A and B samples (Table 3) reflects a different degree of packing of the sediment.

The values for  $\sigma_{DC}$  [equation (7)] range from  $4.31 \times 10^{-3}$  to  $4.54 \times 10^{-3}$  S/m for the humid material, and from  $1.15 \times 10^{-4}$  to  $1.91 \times 10^{-4}$  S/m for the dry material (Table 3). The higher conductivities for the humid samples are caused by the water that occupies part of the pore space, replacing the nonconductive air. We observed that  $\sigma_{DC}$  showed no trend related to the iron-oxide units. It follows that the amount of iron oxides does not affect the conductivity of the samples enough to create significant impedance changes between the samples [equation (1)]. Similar conductivity values were found for a sediment with 10% iron oxides by weight from Meerske, The Netherlands

(J. Reckman, 2000, private communication). The conductivity of this sediment, with a density of 2240 kg/m<sup>3</sup>, was measured to be around  $2 \times 10^{-4}$  S/m.

The calculated  $\varepsilon_r$  values for the humid A samples range from 5.12 to 7.62, and show a positive correlation with the amount of iron oxides in the sediment (Table 3). Using dielectric mixing models [equations (5) and (6)], we estimated the influence of the different phases (solid, water, gas) on  $\varepsilon_r$ . The calculated values for  $\varepsilon_s$ , which lie in a narrow range of about 3.6 to 3.8, with one peak at 4.1 (Table 3), show no correlation with bulk density, water content, and iron-oxide content. The observed spreading of  $\varepsilon_r$  values falls within the expected range (Roth et al., 1990) and cannot be interpreted in more detail because we did not measure the sample temperatures, we do not know the exact density of the solid phase, and because of the accuracy limitations of the TDR equipment. The calculations using the dielectric mixing model show that iron oxides do not directly alter  $\varepsilon_r$ , by changing  $\varepsilon_s$ . Instead, the variation in  $\varepsilon_r$ ,  $\mu_r$  is caused by changes in volumetric water content, positively correlated with the amount of iron oxides in the sediment (Table 3).

## DISCUSSION

### Iron-oxide material

The ICP-AES measurements of iron content and the 200–300°C weight loss in the TGA measurements show a strong crosscorrelation ( $R^2 = 0.97$ ) and a strong correlation with the three units (Table 1). We assume that both data sets can be used as a proxy for the amount of iron oxides in the sediment. A crossplot of relative magnetic permeability ( $\mu_r$ ) and the 200–300°C weight loss shows a good correlation (Figure 5). An exponential trendline was fitted to the data satisfactorily ( $R^2 = 0.82$ ) on an empirical basis. The plot confirms the observation that these variables are controlled by the amount of iron oxides present. Using the information from both measurements and data from Blazek (1973) and Mullins (1977), the type of iron oxide can be determined (Table 4). As the samples

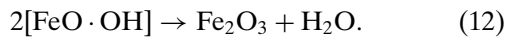
**Table 1. Description of samples.**

Sample code (Figure 1)	Unit	Grain size		ICP	TGA			
		Size ( $\mu\text{m}$ )	Sd*	Fe content (ppm)	Weight (g)	Sub 105°C weight loss (%)	200–300°C water-corrected weight loss (%)	400–600°C weight loss (%)
OS5a-8/9	White	248.8	119.9	1485.8	78.92	3.152	0.029	0.110
OS5a-11/12	White	239.3	123.1	1988.9	55.82	1.809	0.042	0.165
OS11-5	White	282.6	133.6	980.2	72.01	9.221	0.026	0.084
Bulk-whi_A	White	274.8	135.4	992.9	66.44	3.217	0.028	0.096
Bulk-whi_B	White	271.4	133.7	1296.8	89.76	3.825	0.028	0.114
OS5a-1/2	Orange	256.7	126.4	2013.6	64.04	4.265	0.052	0.130
OS5a-3/4	Orange	269.6	133.5	2431.6	80.09	3.698	0.044	0.121
OS8-1	Orange	298.8	149.2	2162.4	103.30	4.093	0.033	0.099
OS8-3	Orange	248.9	132.8	2708.6	46.28	1.239	0.055	0.156
OS11-1	Orange	337.2	163.6	1751.9	69.13	4.149	0.035	0.099
OS11-4	Orange	307.1	149.5	1951.9	76.04	7.614	0.036	0.090
Bulk-ora_A	Orange	246.6	122.9	2829.9	91.02	5.325	0.056	0.130
Bulk-ora_B	Orange	244.4	122.1	2743.6	84.14	5.516	0.056	0.124
OS5a-6/7a	Red	283.8	143.3	5762.5	66.68	4.668	0.118	0.136
OS5a-6/7b	Red	260.2	128.5	5947.0	88.33	10.064	0.122	0.144
OS8-2	Red	272.3	138.6	4223.1	60.94	5.069	0.085	0.121
OS11-2	Red	360.8	167.2	7050.1	55.16	7.287	0.151	0.112
OS11-3	Red	271.2	131.0	5551.0	66.00	7.634	0.105	0.104
Bulk-red_A	Red	325.5	157.7	6450.4	87.75	6.244	0.122	0.107
Bulk-red_B	Red	326.5	157.0	6181.5	82.43	5.756	0.101	0.099

\*Sd = standard deviation.

are composed of several compounds (grains, pore gas, and water), the mass-specific susceptibility ( $\chi$ ) is a mixed number. Regarding the very low  $\chi$  values measured (Table 2), the iron oxides cannot be of ferrimagnetic type such as magnetite or maghemite (Table 4). Antiferromagnets and paramagnets do have the required low susceptibility. Of these, hematite drops out because its DTG peak occurs at a temperature higher than the observed 280°C (Table 4). The  $\alpha$ - and  $\gamma$ -FeO·OH type iron oxides as well as ferrihydrite, which have the required thermal characteristics, generally occur simultaneously. However, of these, goethite is most common and can be expected to be the main constituent of the iron-oxide material (Robinson et al., 1994; Cornell and Schwertmann, 1996).

The reaction that occurs for FeO·OH-type iron oxide at 280°C is dehydroxylation (Dekkers, 1990):



This loss of water causes the measured weight loss. Under normal measurement conditions, the nonpolar OH molecules are strongly bound in the crystalline structure and cannot account

for the variation in dielectric properties as observed in the Ossendrecht TDR measurements.

**Volumetric water content**

The magnetic and TDR measurements showed that the goethite has a minor influence on  $\mu_r$ , and that the iron oxides do not significantly change the conductivity or the relative permittivity ( $\epsilon_s$ ) of the grains (Table 3). The TG measurements showed that  $\theta$  is significantly higher for sediments containing iron oxides (Figure 2). Figure 6, which plots iron-oxide content (approximated by the iron content from the ICP-AES measurements) against free-water-related weight loss, shows a clear and positive correlation, although the orange and white units show some overlap (Table 1). Goethite thus appears to retain more water in the sediment, causing an increase in  $\epsilon_r$ . The observed variations in dielectric properties (Figure 1) can thus be explained by changes in free-water content. It is important to understand these differences in  $\theta$  and  $\epsilon_r$ , which can alter the behavior of electromagnetic and GPR waves.

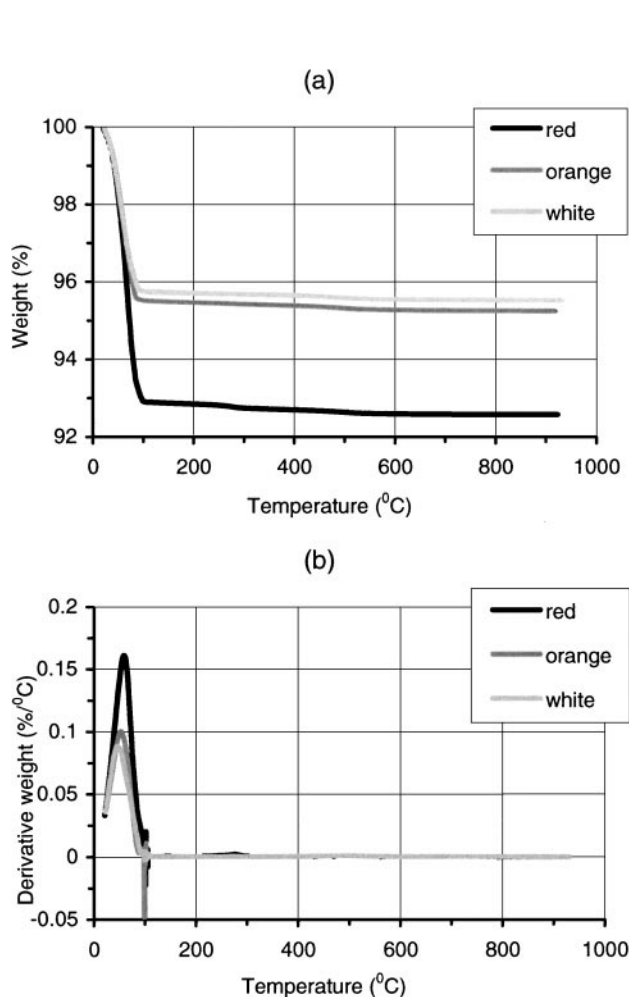


FIG. 2. Results of TG analysis. All weights are expressed in percentage of total weight to facilitate comparison. The TG curves (a) plot the sample weight against temperature, whereas the derivatives of these curves (b) show weight change (averaged over 10 measurement points) against temperature. The color indications refer to the units defined in Figure 1 and Table 1.

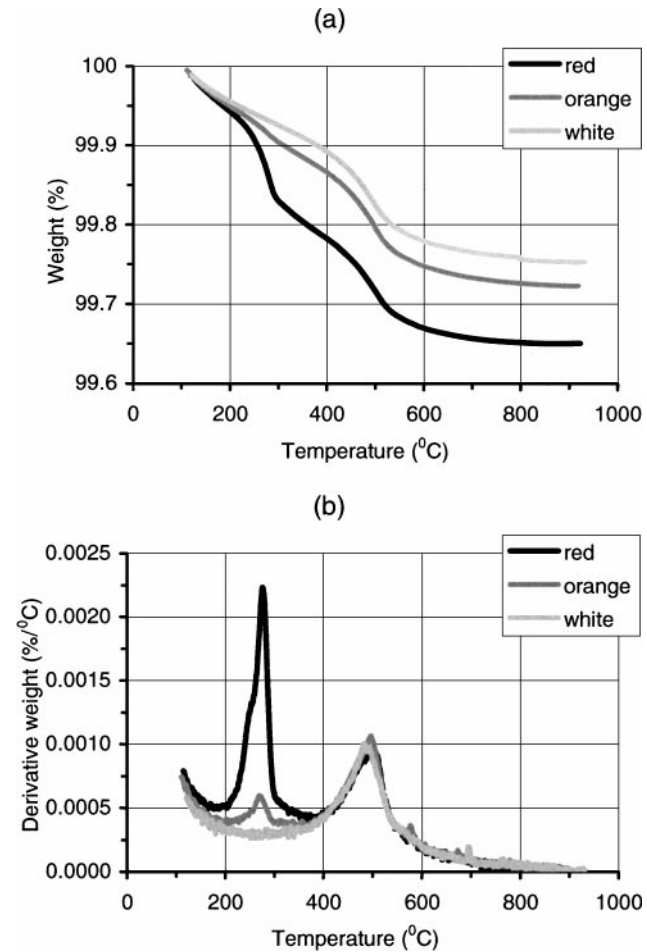


FIG. 3. TG curves (a) and their derivatives (b) showing the results of thermogravimetric analysis after correction for the free-water content, focussing on the thermal behavior of the samples for the temperature range above 100°C. The weights have been set to 100% at a temperature of 105°C to enable comparison. The DTG curves were calculated as an average over 10 measurement points. The color indications refer to the units defined in Figure 1 and Table 1.

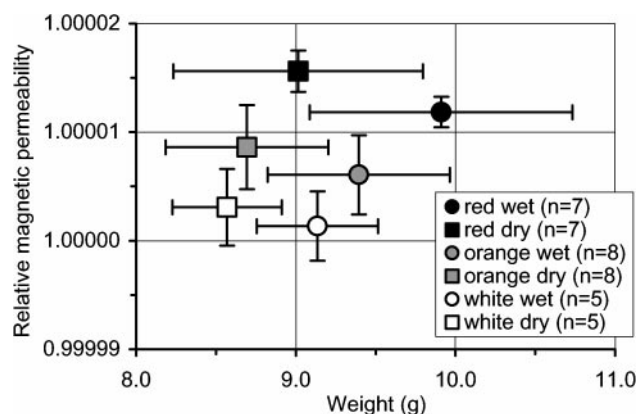


FIG. 4. Results of magnetic measurements using a bridge-type susceptometer. The relative magnetic permeability ( $\mu_r$ ) is plotted against sample weight. The measurements have been separated into white, orange, and red units, and were measured under both field conditions (i.e., humid) and after drying. The rods give the standard deviations of the measurements. The color indications refer to the units defined in Figure 1 and Table 1.

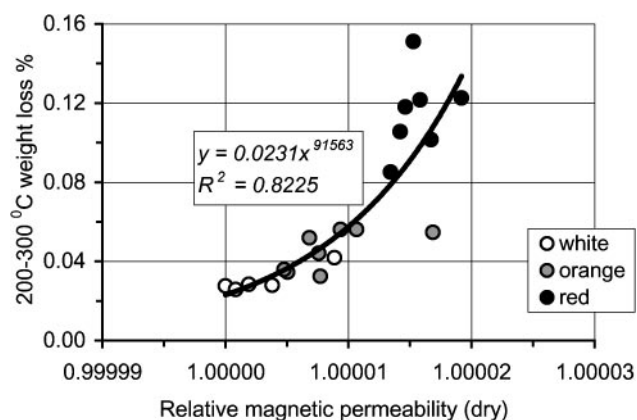


FIG. 5. A cross plot of the 200 to 300°C weight loss % from the TG measurements and the relative magnetic permeability ( $\mu_r$ ). The diagram shows a positive correlation, illustrated by the correlation coefficient of the fitted power function, related to the amount of iron oxides in the sediment. The color indications refer to the units defined in Figure 1 and Table 1.

**Table 2. Results of magnetic susceptibility measurements. The symbols represent mass-specific susceptibility ( $\chi$ ) and relative magnetic permeability ( $\mu_r$ ).**

Sample code	Unit	Humid samples			Dry samples		
		Weight (g)	$\chi$ ( $10^{-8}$ m <sup>3</sup> /kg)	$\mu_r$	Weight (g)	$\chi$ ( $10^{-8}$ m <sup>3</sup> /kg)	$\mu_r$
OS5a-8/9	White	9.35	0.06844	1.0000171	8.70	0.15284	1.0000382
OS5a-11/12	White	8.99	0.26690	1.0000667	8.44	0.35438	1.0000886
OS11-5	White	9.09	-0.03574	0.9999911	8.45	0.03374	1.00000843
Bulk-whi_A	White	8.62	-0.04583	0.9999885	8.18	0.00061	1.00000015
Bulk-whi_B	White	9.62	0.01662	1.0000042	9.08	0.07595	1.0000190
OS5a-1/2	Orange	8.51	0.19925	1.0000498	8.04	0.27300	1.0000683
OS5a-3/4	Orange	9.30	0.20854	1.0000521	8.71	0.30318	1.0000758
OS8-1	Orange	8.83	0.20263	1.0000507	8.12	0.30926	1.0000773
OS8-3	Orange	9.28	0.54734	1.0001368	8.67	0.67443	1.0001686
OS11-1	Orange	9.55	0.11258	1.0000281	8.85	0.20294	1.0000507
OS11-4	Orange	9.40	0.07552	1.0000189	8.42	0.19116	1.0000478
Bulk-ora_A	Orange	10.22	0.28858	1.0000721	9.50	0.37455	1.0000936
Bulk-ora_B	Orange	10.06	0.30916	1.0000773	9.24	0.42628	1.0001066
OS5a-6/7a	Red	9.96	0.43719	1.0001093	9.08	0.58553	1.0001464
OS5a-6/7b	Red	8.89	0.57620	1.0001441	7.97	0.76731	1.0001918
OS8-2	Red	8.98	0.41602	1.0001040	8.26	0.53691	1.0001342
OS11-2	Red	10.33	0.48079	1.0001202	9.48	0.61125	1.0001528
OS11-3	Red	9.87	0.38768	1.0000969	8.75	0.56885	1.0001422
Bulk-red_A	Red	11.26	0.48951	1.0001224	10.30	0.63325	1.0001583
Bulk-red_B	Red	10.09	0.53138	1.0001328	9.27	0.66851	1.00016713

**Table 3. Results from the laboratory TDR measurements on bulk material. The symbols represent porosity ( $\eta$ ), bulk density ( $\rho_b$ ), volumetric water content ( $\theta$ ), bulk electrical conductivity ( $\sigma_{DC}$ ), relative permittivity ( $\epsilon_r$ ), and relative permittivity of solid material ( $\epsilon_s$ ).**

Sample code	Unit	Status	Textural properties				Dielectric properties		
			Weight (g)	$\eta$	$\rho_b$ (g/cm <sup>3</sup> )	$\theta$	$\sigma_{DC}$ (S/m)	$\epsilon_r$	$\epsilon_s$
Bulk-whi_A	White	Humid	309.28	0.418	1.546	0.092	0.00431	5.119	3.643
Bulk-ora_A	Orange	Humid	323.36	0.402	1.617	0.122	0.00454	6.290	3.599
Bulk-red_A	Red	Humid	330.56	0.396	1.653	0.144	0.00448	7.616	4.099
Bulk-whi_A	White	Dry	290.80	0.418	1.454	–	0.000151	2.309	3.584
Bulk-ora_A	Orange	Dry	298.90	0.402	1.495	–	0.000137	2.439	3.763
Bulk-red_A	Red	Dry	301.83	0.396	1.509	–	0.000115	2.451	3.751
Bulk-whi_B	White	Dry	283.68	0.433	1.418	–	0.000171	2.389	3.848
Bulk-ora_B	Orange	Dry	289.50	0.421	1.448	–	0.000191	2.385	3.764
Bulk-red_B	Red	Dry	278.11	0.444	1.391	–	0.000178	2.276	3.666

The volumetric water content ( $\theta$ ) for the samples used in the TDR laboratory measurements (Table 3) ranges from 0.092 to 0.14. Using the empirical relationship given by Topp et al. (1980), the field measurements of  $\epsilon_r$  (Figure 1) give  $\theta$  values between 0.055 and 0.17. The values show that the water occupies a maximum of around one third of the pore volume (Table 3), predominantly stored as capillary water in small pore bodies and pore throats. The amount of water that can be retained as capillary or free water depends on the capillary pressure and pore shape (De Marsily, 1986). The amount of water that can be retained as adhesive water, which has a relative permittivity lower than that of free water (Roth et al., 1990), depends on the specific surface of the sediment, but is small compared to the maximum amount of capillary water.

It is shown in various studies using SEM that iron-oxide minerals have a relatively rough surface texture relative to quartz grains (e.g., Frank, 1981; Smart and Tovey, 1981; Welton, 1984). Iron-oxide minerals like goethite appear to have a larger specific surface than quartz, which allows for more adhesive wa-

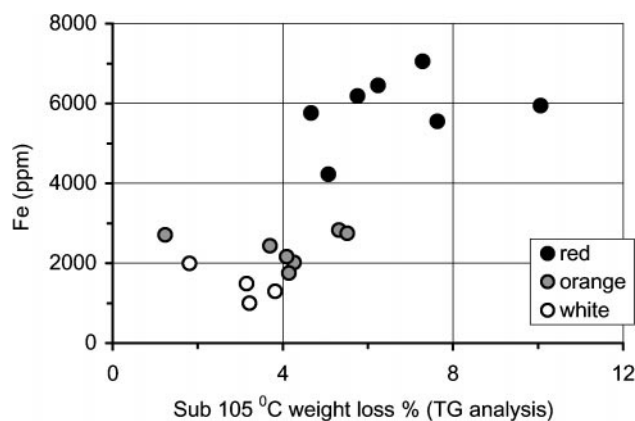


FIG. 6. A crossplot of the iron content from ICP measurements and the free-water related weight loss during drying below 105°C from the TG analysis. The iron content is a proxy for the amount of iron oxides in the samples (see text). Although all samples were taken under similar conditions from nearby positions, small differences in grain size or time of exposure to air may have changed the amount of free water in the samples. This might explain the relatively large variation in weight-loss percent. Samples OS11-4 and OS11-5 have been omitted from the diagram because their water content was strongly influenced by the close water table. The diagram shows a positive correlation, related to the amount of iron oxides in the sediment. The color indications refer to the units defined in Figure 1 and Table 1.

Table 4. Thermal behavior and magnetic susceptibilities for several iron oxides and soil constituents. Data from Blazek (1973), Mullins (1977), Thompson and Oldfield (1986), Cornell and Schwertmann (1996), and Maher (1998). The symbol  $\chi$  = mass-specific susceptibility.

Material	Chemical formula	Magnetic status	$\chi$ ( $10^{-8}$ m <sup>3</sup> /kg)	Thermal peak temperature (°C)
Ferrihydrite	Fe <sub>2</sub> O <sub>3</sub> .xH <sub>2</sub> O	Paramagnetic	~40	125–500
Goethite	$\alpha$ -FeO·OH	Antiferromagnetic	12.5–126	200–400
Hematite	$\alpha$ -Fe <sub>2</sub> O <sub>3</sub>	Antiferromagnetic	27–63	1360–1440
Lepidocrocite	$\gamma$ -FeO·OH	Paramagnetic	50–75	275–410
Maghemite	$\gamma$ -Fe <sub>2</sub> O <sub>3</sub>	Ferrimagnetic	26000–44000	510–570
Magnetite	Fe <sub>3</sub> O <sub>4</sub>	Ferrimagnetic	39000–100000	275–371
Quartz	SiO <sub>2</sub>	Diamagnetic	-0.58	573
Water	H <sub>2</sub> O	Diamagnetic	-0.9	100

ter to be present per unit volume of sediment. At a larger scale, the increased surface roughness of the grains, due to the growth of iron-oxide minerals, will create niches that free water can occupy. These features explain the correlation between iron-oxide content, free-water content, and dielectric properties that was observed in the Ossendrecht samples.

## GPR

It is now obvious that, as long as the sediment contains water, variation in the abundance of iron oxides in the sediment can have a significant influence on  $\epsilon_r$ , and, thus, the electromagnetic signal. To understand the influence on the GPR signal, we constructed synthetic 2-D radar sections for which we used  $\epsilon_r$  values obtained during the laboratory TDR measurements (Table 5) and a  $\mu_r$  of 1 (Table 2). Theoretically, a higher  $\theta$  will result in more attenuation ( $\alpha$ ), but to keep the model elementary, we set the required input for  $\alpha$  to 0.1. We calculated the velocities using equation (2). The results in Table 5 show that the velocities range from 0.095 m/ns for red (iron-oxide rich) fine sand with iron oxides to 0.133 m/ns for white sand. As iron-oxide precipitation is a diagenetic process, the flow paths of the pore water play an important role in the formation and morphology of iron-oxide rich zones. These flow paths are influenced by a number of factors, such as sedimentary structures, discontinuities, and regional flow patterns. Based on these factors, we selected three field examples (Figure 7), that we translated into velocity models using the data given in Table 5. These models, in turn, are input for the 2-D ray-trace modeling software.

Table 5. Electromagnetic wave velocities for a range of observed relative permittivities in field and lab, as well as estimates for fine sand (that was used for the GPR modeling) and some reference materials.

	Relative permittivity ( $\epsilon_r$ )	Velocity (m/ns)
Minimum observed field	4.0	0.150
Maximum observed field	9.0	0.100
White sand laboratory	5.1	0.133
Orange sand laboratory	6.3	0.120
Red sand laboratory	7.6	0.109
White fine-sand estimate	5.3	0.130
Orange fine-sand estimate	6.8	0.115
Red fine-sand estimate	10.0	0.095
Air	1.0	0.300
Saturated sand	25.0	0.060
Water	80.0	0.034

The simplest situation is where the precipitates follow original cross-bedding or bounding surfaces, as in Bristow (1995). The example in Figure 7a (based on site 5a in Figure 1) shows precipitates that were formed on a bounding surface. It is important to note that the top reflection (from the transition of orange to red sand) would not occur under a situation without an iron-oxide-enriched layer. The bottom reflection (red to white sand) has a higher amplitude than can be expected from the grain size variation at the bounding surface alone.

Figure 7b shows a situation where an iron-oxide band (made up of an orange upper part and a red lower part) crosscuts de-

positional bedding (field example given in Figure 5 of Van Dam and Schlager, 2000). The depositional bedding is represented by a 0.2-m thick fine-sand layer within coarser sand. The fine sand, containing more (capillary) water than the coarse sand, forms a low-velocity zone. An important feature to note is the nonhorizontal morphology of the top and bottom reflections of this layer in the resulting radar section. The top reflection of the fine-sand layer dips gradually to the right, whereas the bottom reflection is concave up. This feature is due to the velocity push-down by the iron-oxide rich material. The bottom reflection of the fine-sand layer loses amplitude towards the

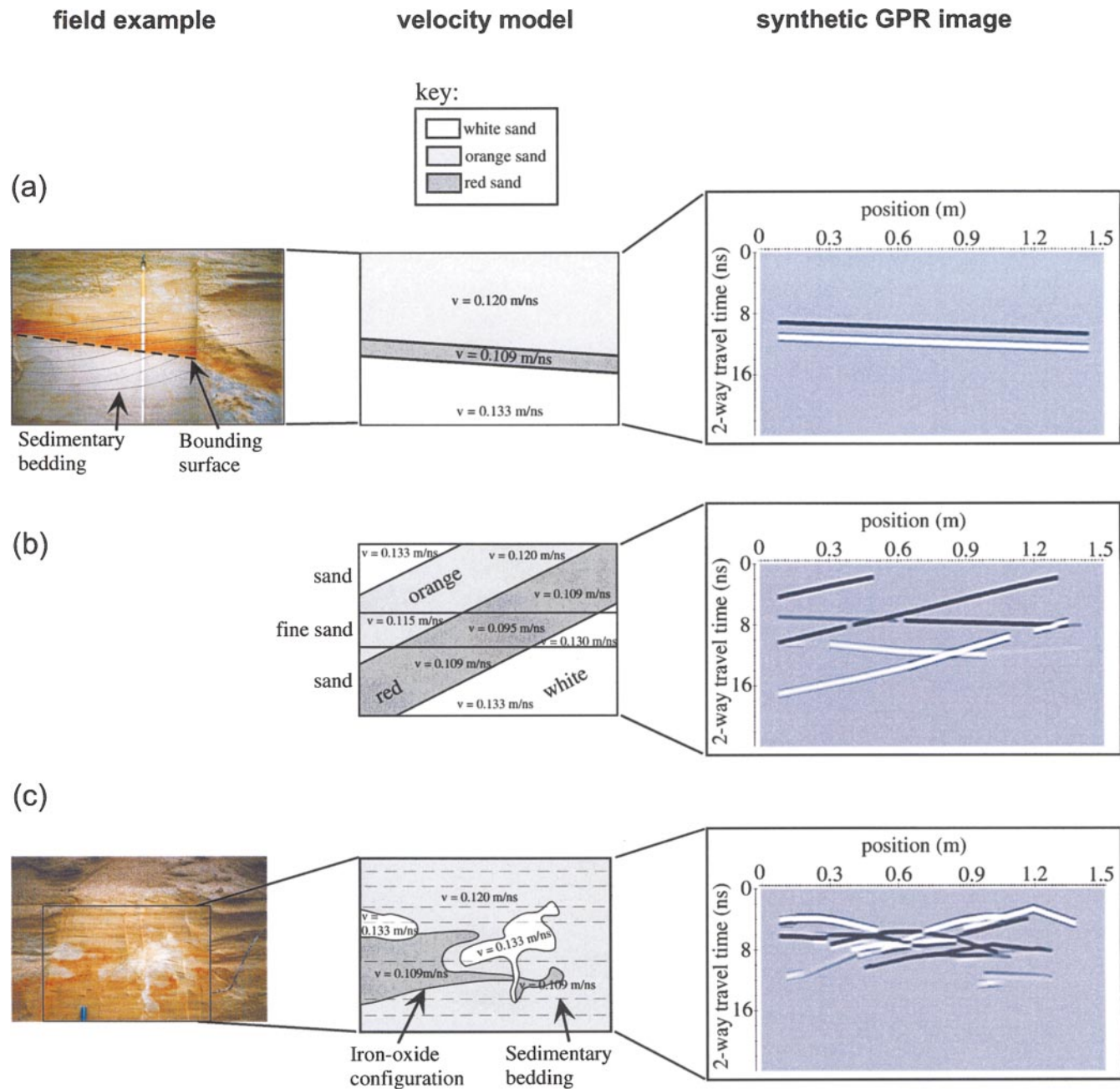


FIG. 7. Selected field examples of iron-oxide precipitates, velocity models, and 2-D synthetic ray-trace GPR images: (a) precipitates that follow original bedding; (b) precipitates that crosscut original bedding; and (c) discontinuities. The examples have dimensions of 1.5 m wide and 1 m high. The GPR synthetic radar sections were constructed using a Ricker wavelet and a 900-MHz frequency.

right, due to the low velocity contrast between white fine and normal sand. A real GPR section will show more complexity due to diffraction hyperbolas that form at intersections.

An example of iron oxide that precipitated irregularly is given in Figure 7c. Here, the sedimentary bedding is horizontal. The velocity model is a simplified representation of this situation. The synthetic radar section shows the difficulty in reconstructing the original reflector morphology from the reflection configuration.

### CONCLUSIONS

This study began with the premise that iron oxides might influence GPR performance. Field data showed that iron oxides lower the electromagnetic wave velocity in sediments. For a set of samples containing a varying amount of precipitated goethite, we carefully analyzed all parameters that influence electromagnetic wave behavior. Magnetic measurements showed that the relative abundance of iron oxides influences relative magnetic permeability consistently, but the variation is too small to be significant for electromagnetic wave behavior. Time-domain reflectometry measurements on bulk samples under field (humid) and dry conditions showed that the electrical conductivity did not vary systematically with iron-oxide content. Using the dielectric mixing models we demonstrated that the iron oxides do not alter the relative permittivity of the solid phase in the sediment. Thus, none of the three components of electromagnetic waves ( $\mu$ ,  $\sigma$ , and  $\epsilon$ ) is directly influenced by the iron oxides. However, the sub-105°C weight-loss percentage during the thermogravimetric analysis showed that the amount of iron oxide in the material is correlated with the volumetric water content and, thus, the dielectric properties of the samples. The correlation is caused by the larger specific surface and capillary retention capacity of iron oxides like goethite, as compared with quartz grains. Iron oxides thus can have a profound influence on the relative permittivity and, consequently, the GPR signal. Depending on the morphology and precipitation pattern, the iron-oxide zones may either exaggerate individual reflections, cause an increased attenuation, or complicate reflection configurations and interpretation of GPR images.

### ACKNOWLEDGMENTS

We thank Prof. Poppe De Boer and Marjan Reith (Utrecht University, Earth Sciences) for their permission to use and operation of the TG equipment, respectively. We thank Saskia Kars for performing the SEM and EDX measurements, and Pieter Vroon, Roel Van Elsas, and Richard Smeets for assistance with the ICP-AES. We also thank Kay Beets for his useful suggestions, and Erwin Adams for commenting on an earlier version of the text. We are grateful to Steve Arcone and Joseph Kruger for their valuable suggestions to improve the manuscript.

### REFERENCES

- Blazek, A., 1973, Thermal analysis: Van Nostrand Reinhold Co.
- Bohl, H., and Roth, K., 1994, Evaluation of dielectric mixing models to describe the  $\theta(\epsilon)$ -relation: Time domain reflectometry in environmental, infrastructure and mining applications, U.S. Bur. Mines Spec. Pub. 19-94, 309-317.
- Brewster, M. L., and Annan, A. P., 1994, Ground-penetrating radar monitoring of a controlled DNAPL release: 200 mHz radar: *Geophysics*, **59**, 1211-1221.
- Brisco, B., Pultz, T. J., Brown, R. J., Topp, G. C., Hares, M. A., and Zebchuck, W. D., 1992, Soil moisture measurement using portable dielectric probes and time domain reflectometry: *Water Resources Research*, **28**, 1339-1346.
- Bristow, C. S., 1995, Facies analysis in the Lower Greensand using ground-penetrating radar: *J. Geol. Soc.*, **152**, 591-598.
- Carcione, J. M., 1998, Radiation patterns for 2-D GPR forward modeling: *Geophysics*, **63**, 424-430.
- Cornell, R. M., and Schwertmann, U., 1996, The iron oxides—structure, properties, reactions, occurrence and uses: VCH Publishers.
- Daniels, D. J., Gunton, D. J., and Scott, H. E., 1988, Introduction to subsurface radar: *IEE Proceedings*, **135**, 278-320.
- Davis, J. L., and Annan, A. P., 1989, Ground-penetrating radar for high resolution mapping of soil and rock stratigraphy: *Geophys. Prosp.*, **37**, 531-551.
- Dekkers, M. J., 1990, Magnetic properties of natural goethite-III. Magnetic behaviour and properties of minerals originating from goethite dehydration during thermal demagnetization: *Geophys. J. Internat.*, **103**, 233-250.
- De Marsily, G., 1986, Quantitative hydrogeology: Academic Press Inc.
- Driessen, P. M., and Dudal, M., 1991, The major soils of the world: Koninklijke Wöhrmann B.V.
- Földvari, M., 1991, Measurement of different water species in minerals by means of thermal derivatography, *in* Smykatz-Kloss, W., and Warne, S. S. J., Eds., Thermal analysis in geosciences: Springer-Verlag Berlin, 84-101.
- Frank, J. R., 1981, Dedolomitization in the Taum Sauk limestone (Upper Cambrian), southeast Missouri: *J. Sedim. Petr.*, **51**, 7-18.
- Giese, K., and Tieman, R., 1975, Determination of the complex permittivity from thin-sample time domain reflectometry: Improved analysis of the step response waveform.: *Adv. Mol. Rel. Proc.*, **7**, 45-59.
- Huggenberger, P., 1993, Radar facies: Recognition of facies patterns and heterogeneities within Pleistocene Rhine gravels, NE Switzerland, *in* Best, J. L., and Bristow, C. S., Eds., Braided rivers: *Geol. Soc. London*, 163-176.
- Huisman, J. A., and Bouten, W., 2000, Comparison of calibration and direct measurement of cable and probe properties in time domain reflectometry: *Soil Sci. Soc. Am. J.*, **63**, 1615-1617.
- Klein, K., and Santamarina, J. C., 2000, Ferromagnetic inclusions in geomaterials: implications: *J. Geotechn. Geoenvironm. Eng.*, **126**, 167-179.
- Maher, B. A., 1998, Magnetic properties of modern soils and Quaternary loessic paleosols: Paleoclimatic implications: *Palaeogeography Palaeoclimatology Palaeoecology*, **137**, 25-54.
- Mätzler, C., 1998, Microwave permittivity of dry sand: *IEEE Trans. Geosci. Remote Sensing*, **36**, 317-319.
- Mullins, C. E., 1977, Magnetic susceptibility of the soil and its significance in soil science—A review: *J. Soil Sci.*, **28**, 223-246.
- Robinson, D. A., Bell, J. P., and Batchelor, C. H., 1994, Influence of iron minerals on the determination of soil water content using dielectric techniques: *J. Hydrology*, **161**, 169-180.
- Roth, K., Schulin, R., Flühler, H., and Attinger, W., 1990, Calibration of time domain reflectometry for water content measurement using a composite dielectric approach: *Water Resources Research*, **26**, 2267-2273.
- Smart, P., and Tovey, N. K., 1981, Electron microscopy of soils and sediments: examples: Oxford Univ. Press, Inc.
- Sutinen, R., 1992, Glacial deposits, their electrical properties and surveying by image interpretation and ground penetrating radar: Ph.D. thesis, University of Oulu.
- Thompson, R., and Oldfield, F., 1986, Environmental magnetism: Allen & Unwin.
- Tinga, W. R., Voss, W. A. G., and Blossey, D. F., 1973, Generalized approach to multiphase dielectric mixture theory: *J. Appl. Phys.*, **44**, 3897-3902.
- Topp, G. C., Davis, J. L., and Annan, A. P., 1980, Electromagnetic determination of soil water content: Measurements in coaxial transmission lines: *Water Resources Research*, **16**, 574-582.
- Ulriksen, C. P. F., 1982, Application of impulse radar to civil engineering: Ph.D. thesis, Lund Univ. of Technology.
- Van Dam, R. L., and Schlager, W., 2000, Identifying causes of ground-penetrating radar reflections using time-domain reflectometry and sedimentological analyses: *Sedimentology*, **47**, 435-449.
- Van Der Kruk, J., Slob, E. C., and Fokkema, J. T., 1999, Background of ground-penetrating radar measurements: *Geologie en Mijnbouw*, **77**, 177-188.
- Von Hippel, A. R., 1954, Dielectric materials and applications: John Wiley & Sons, Inc.
- Welton, J. E., 1984, SEM petrology atlas: Am. Assn. Petr. Geol.
- Worm, H.-U., Clark, D. A., and Dekkers, M. J., 1993, Magnetic susceptibility of pyrrhotite: Grain size, field and frequency dependence: *Geophys. J. Internat.*, **114**, 127-137.